Journal of Chromatography A 1721 (2024) 464815

Contents lists available at ScienceDirect

Journal of Chromatography A

journal homepage: www.elsevier.com/locate/chroma

Development, characterization and application of 3D printed adsorbents for in situ recovery of taxadiene from microbial cultivations

Giuseppe Rafael Galindo-Rodriguez [a], M. Sulaiman Sarwar [a], Leonardo Rios-Solis [a,b,1], Simone Dimartino [a,*]

[a] Institute for Bioengineering, School of Engineering, The University of Edinburgh, Edinburgh EH9 3BF, United Kingdom
[b] Centre for Engineering Biology, The University of Edinburgh, Edinburgh EH9 3BF, United Kingdom

ARTICLE INFO

Keywords:
3D printing
Taxadiene
In situ product recovery
Solid adsorption
Downstream processing
Saccharomyces cerevisiae

ABSTRACT

Microbial cell factories are an attractive alternative to produce high-value natural products using sustainable processes. However, product recovery is one of the main challenges to reduce production cost and make these technologies economically interesting. In this work, new resins were formulated to 3D print hydrophobic adsorbents for the recovery of biologics from microbial cultivations. Benzyl methacrylate (BEMA) and butyl methacrylate (BUMA) were selected as functional monomers suitable for the adsorption of hydrophobic compounds. Pore morphology was tailored through the inclusion of pore forming agents (porogens) in the resin. Different porogens and porogen concentrations were evaluated resulting in materials with different porous networks. Sudan 1 and the anticancer drug paclitaxel were employed as model compounds to test the adsorption performance of hydrophobic and terpene molecules onto the developed 3D printed materials. The material with greatest adsorption capacity was obtained using BEMA monomer with 40 % (v/v) porogen (BEMA40). The performance of BEMA40 to recover taxadiene from small-scale (5 mL) *Saccharomyces cerevisiae* cultivations was tested and compared with commercial Diaion HP-20 beads. Taxadiene titres on BEMA40 (46 ± 2 mg/L) and Diaion HP-20 (54 ± 4 mg/L) were comparable, with no taxadiene detected in the cells and cell-free media, suggesting near 100 % taxadiene partition on the adsorbents. Compared to commercial beads, 3D printed adsorbents can be customized with adjustments in the resin formulation, are well adaptable to diverse bioreactor types, do not clog sampling ports and columns and are easier to handle during post processing. The results of this work demonstrate the potential of 3D printing to fabricate hydrophobic interaction adsorbent materials and their application in the recovery of biological products.

1. Introduction

Plant derived natural products have numerous applications and commercial value in the food and pharmaceutical industries [1]. Unfortunately, plant extraction of high-value products like paclitaxel and other compounds is unsustainable due to the low yield, e.g. an entire tree is typically required to obtain a few grams of product [2]. Ultimately over 15,000 medicinal plants are endangered through over-exploitation due to their high demand and rarity [3].

Microbial cell factories present a sustainable alternative for manufacturing natural products since they offer a relatively high yield without damaging the local environment [4–6]. Research on microbial cell factories has mainly focused on upstream strategies to produce high levels of the desired product, such as developing or improving microbial strains, as well as optimization of culture media and process parameters [2,7–9]. However, less attention has been paid to the downstream portion concerning product recovery which accounts for up to 80 % of the total production cost [8].

A common method employed for recovery in downstream processing involves dispersing beads inside the fermenter which adsorb the product of interest [10]. Typically, taxadiene has been recovered from culture media using commercial adsorbent beads like Diaion HP-20 beads, a macroporous polymeric resin made of poly(styrene-co-divinylbenzene) [11–13]. However, during agitation these beads induce shear stress on

* Corresponding author.
E-mail address: simone.dimartino@ed.ac.uk (S. Dimartino).
[1] Current address: Department of Biochemical Engineering, The Advanced Centre for Biochemical Engineering, University College London, London, WC1E 6 EB United Kingdom

https://doi.org/10.1016/j.chroma.2024.464815
Received 25 January 2024; Received in revised form 6 March 2024; Accepted 11 March 2024
Available online 19 March 2024

the cells which inhibits cell growth. Moreover, the beads degrade during operation since the impeller changes their surface and adsorption capacity [14–16].

In recent years, the use of monolithic structured adsorbents has attracted attention to substitute particle-shaped adsorbents [17–19]. Compared to beads, structured adsorbents have little effect on cell growth kinetics and are significantly more stable. At the state-of-the-art, 3D-printing technologies such as digital light processing (DLP) can be used to fabricate monoliths with varying physicochemical properties and adapt these materials for different bioreactor types and configurations. In DLP printing, structures are built in layers by projecting images of a computer aided design (CAD) model onto a photosensitive resin [20, 21]. The photopolymerisable resin is highly customisable and can be formulated with monomers (either mono or multi-functional), cross-linkers, porogens, a photoinitiator and a photoabsorber [22].

Methacrylate- and acrylate-based monomers are widely used in photopolymerisation since they contain double bonds which readily react with each other in the presence of radicals [23]. Methacrylates have excellent biocompatibility and are less toxic than acrylates, therefore more suitable for bioprocessing applications [24]. In addition, methacrylate polymers are endowed with excellent chemical resistance and mechanical properties, which makes them a material of choice in a range of biological applications, from biomedical [25] to bioprocessing [18,26,27].

In this study, 3D printed adsorbents were developed and applied in an integrated process to simultaneously produce and recover taxadiene in *S. cerevisiae* cultivations. For our 3D-printable monoliths we selected benzyl methacrylate (BEMA) as viable monomer for use in DLP printing to fabricate adsorbent materials displaying benzene rings in its structure to resemble styrene-DVB resins (Fig. 1). Furthermore, butyl-methacrylate (BUMA) was included in the resin formulation to impart more hydrophobic behaviour to the materials. Pore size was modulated by: (1) adjusting the porogen concentration to 30, 40 and 60 % (v/v) in the resin composition and (2) using alternative co-porogen mixtures. Batch adsorption equilibrium and kinetic experiments were carried out to determine the material with the highest adsorption performance. The optimal material was then used in *S. cerevisiae* cultivations to recover taxadiene and compared to the commercial bead-based alternative.

2. Materials and methods

2.1. Materials

Benzyl methacrylate (BEMA), butyl methacrylate (BUMA), (*R*)-(+)-limonene, paclitaxel (≥99.5 %), Sudan 1, phenyl bis(2,4,6-trimethylbenzoyl)-phosphine oxide (Omnirad 819), isopropanol, cyclohexanol (CyOH), dodecanol (DoOH), peptone from casein, glucose and galactose were obtained from Sigma-Aldrich (St. Louis, MO, USA). Yeast extract, Diaion HP-20, acetone and dodecane were obtained from Fisher Scientific (Loughborough, UK). Di-pentaerythritol pentaacrylate (SR399) was kindly donated by Arkema-Sartomer (Colombes, France). Tinuvin 326 was kindly provided by BASF (Ludwigshafen, Germany). All chemicals were used as received.

2.2. Yeast strain

The *S. cerevisiae* strain used in this study was *LRS5 {mGTy116; ARS1014::GAL1p-TASY-GFP; ARS1622b::GAL1p-MBP-TASY-ERG20; ARS1114a::TDH3p-MBP-TASY-ERG20}* as previously described in [7]. This strain was originally derived from the CEN.PK2–1C laboratory (EUROSCARF, Oberursel, Germany). The strain was maintained and stored in glycerol at −80 °C.

2.3. Resin formulations

Resin compositions containing 30, 40 and 60 % (v/v) porogen were formulated to fabricate 3D adsorbent materials with varying pore structure. In these resins, only the monomer/porogen ratio was adjusted to achieve the desired porogen concentration, while the relative ratio between monomers and cross-linkers was kept constant at 45:15:40 for BEMA, BUMA and SR399, respectively. Similarly, the co-porogen used in these resins (CP-1) was a mixture of CyOH and DoOH at a relative ratio of 80:20, respectively. Additionally, a resin with 40 % porogen concentration was prepared with an alternative co-porogen (CP-2) made of CyOH and DoOH at a ratio of 20:80, respectively. The photoinitiator and photoadsorber in all resins were Omnirad 819 and Tinuvin 326 at a concentration of 1 % (w/v) and 0.1 % (w/v), respectively. All resin compositions are summarized in Table 1.

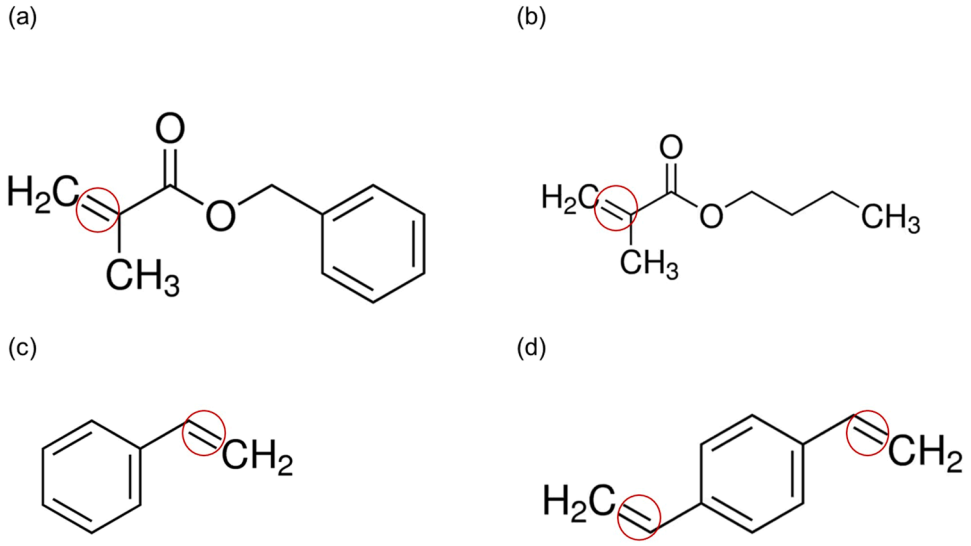

Fig. 1. Comparison of monomers used in the resin composition to fabricate 3D printed adsorbents, BEMA (a) and BUMA (b) with the monomers utilized to prepared Diaion HP-20, copolymer of styrene (c) and divinylbenzene (d). In red are highlighted the vinyl double bonds that react in the presence of radicals during radical polymerisation.

Table 1
Resin compositions prepared with different porogen concentrations, co-porogen type and monomers. Concentration of all components is shown in % v/v.

Resin name	Co-porogen	BEMA	BUMA	SR399	CyOH	DoOH
BEMA30	CP-1	31.5 %	10.5 %	28.0 %	24.0 %	6.0 %
BEMA40	CP-1	27.0 %	9.0 %	24.0 %	32.0 %	8.0 %
BEMA60	CP-1	18.0 %	6.0 %	16.0 %	48.0 %	12.0 %
BEMAP2	CP-2	27.0 %	9.0 %	24.0 %	8.0 %	32.0 %

2.4. Design of adsorbents and 3D printing

A Schoen gyroid (SG) was used as unit cell to model and fabricate the 3D printed adsorbents. The SG was generated using Mathematica 10.4 (Wolfram Research Inc., Champaign, IL, USA), according to Eq. (1):

$$\sin(x) * \cos(y) + \sin(y) * \cos(z) + \sin(z) * \cos(x) = 0 \quad (1)$$

The macroporosity of this structure was 50 %, i.e. the channel and solid wall thicknesses (in the *x, y* and *z* directions) were equal.

The unit cell was exported as an STL file and processed in Netfabb 2021 (Autodesk, San Rafael, CA, USA). The side of the cubic unit cell was set to 2 mm and replicated 3 times in the *x, y* and *z* directions (27 unit cells) to obtain a SG cube of 6 × 6 × 6 mm (Fig. 2a).

All 3D printed models in the present work were fabricated in a Sol-Flex 350 3D printer (W2P Engineering, Vienna, Austria). This 3D printer works with the UV-LED digital light processing (DLP) technology at a wavelength of 385 nm. In this fabrication method, the resin is contained in a reservoir with the projector usually below where each 2D image is projected forming a stack of layers of the cured material (Fig. 2b). The 3D printed model is attached to a building platform that moves bottom-up in the Z-direction until the printing process is completed. The 3D printed model is removed from the building platform and subsequently washed with ethanol 99 % to remove uncured resin (Fig. 2c). The final product is a 3D printed porous material (Fig. 2d).

2.5. Pore size distribution

The pore structure of the 3D printed materials was characterized by scanning electron microscopy (SEM, JSM IT100, JEOL Ltd Japan). All SEM photographs were obtained with an operating voltage of 20 kV and current of 50 mA.

Prior to the analysis, the samples were equilibrated in water and dehydrated with immersion in liquid nitrogen, followed by freeze-drying under vacuum for 24 h. The dried samples were sputter coated (Agar Auto Sputter Coater, Agar Scientific, Stansted, UK) with a 10 nm thick gold layer to improve image quality and resolution.

The pore size distribution was measured applying the method used by Dong *et al.* [28], and using the Local Thickness plug-in for ImageJ software. Detailed description of the method can be found in the supplementary information.

2.6. Surface area

The surface area of the 3D printed adsorbents was measured by nitrogen gas adsorption experiments performed in a surface area analyser instrument (Gemini VII 2390a, Micromeritics, Gloucestershire, UK) run at 77 K. Prior to analysis, the samples were dried as described in Section 2.5, and then grinded into powder. The powdered samples were degassed at 120 °C for 3 h to remove any remaining moisture. Finally, the surface area was calculated by the analysis of the adsorption/desorption behaviour of the samples using the Brunauer-Emmett-Teller (BET) method.

2.7. Adsorption study

Sudan 1 and paclitaxel were employed as the model hydrophobic and terpene molecules to test the adsorption performance of the developed 3D printed materials.

All adsorption experiments were performed in batch mode using 6-well plates containing 5 mL of solution and one gyroid adsorbent per well. The 6-well plates were mounted on a Thermomixer C (Eppendorf, Wesseling, Germany) to keep the temperature and agitation constant (17 °C and 450 rpm, respectively). Solutions were prepared in an ethanol/water solution 50:50 (%, v/v) due to the low miscibility of Sudan 1 and paclitaxel in water.

The concentration of Sudan 1 and paclitaxel was measured using UV–visible spectroscopy (NanoDropTM 2000c, ThermoFisher, Loughborough, UK) at a wavelength of 476 and 240 nm, respectively.

Commercial Diaion HP-20 beads served as a benchmark to compare its loading capacity and adsorption kinetics with the 3D printed adsorbents. The negative control experiments consisted of Sudan 1 and paclitaxel solutions with no adsorbent material in the well plates to ensure that the change in concentration over time was only attributed to the adsorption process.

2.7.1. Batch adsorption experiments

Batch adsorption experiments were run for 26 h and performed at three (10, 50 and 100 ppm) and four (10, 40, 100 and 200 ppm) initial concentrations, for Sudan 1 and paclitaxel, respectively, range where the relationship between concentration and absorbance is linear.

The loading of Sudan 1 and paclitaxel on the adsorbents at time *t*, q_t, was calculated by a mass balance:

$$q_t = \frac{V_s(C_0 - C_t)}{V_a} \quad (2)$$

where C_0 and C_t are the initial adsorbate concentration and adsorbate concentration at time *t* in the bulk solution, respectively, V_s is the volume of the solution, V_a is the volume of the adsorbent (either the gyroid or beads).

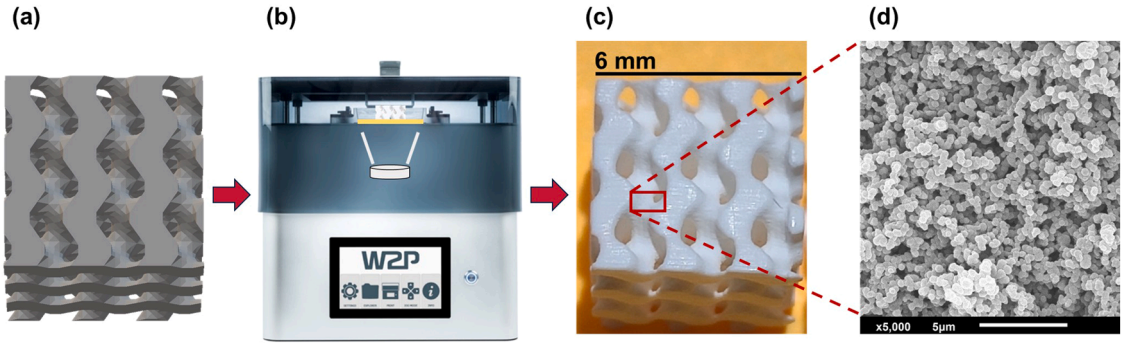

Fig. 2. Diagram displaying the steps to fabricate 3D printed adsorbents. The process involves CAD designing (a) 3D printing (b) and post processing to finally obtain a 3D printed model (c) made of a porous material (d).

2.7.2. Kinetic and mass transfer models in 3D printed adsorbents

Adsorption kinetic experiments were carried out for 26 h with an initial concentration of 100 ppm. Concentration of the solute was measured at 0, 0.1, 0.3, 0.6, 1, 2, 3, 4, 5, 6, 7, 8, 25 and 26 h in Sudan 1 experiments and at 0, 0.3, 0.6, 1, 2, 3, 24 and 26 h in paclitaxel experiments. Loading of Sudan 1 and paclitaxel on the adsorbents was calculated using Eq. (2).

The pseudo first order (PFO, Eq. (3)) and pseudo second order (PSO, Eq. (4)) kinetic models were used to describe the adsorption data under non-equilibrium conditions:

$$q_t = q_e\left(1 - e^{-k_1 t}\right) \tag{3}$$

$$q_t = \frac{k_2 q_e^2 t}{1 + k_2 q_e t} \tag{4}$$

where q_e is the amounts of adsorbate on the adsorbent at equilibrium, and k_1 and k_2 are the rate coefficients for the PFO and PSO models, respectively.

In addition, a pore diffusion model was also evaluated. Pore diffusion assumes that intra-particle mass transfer is governed by the concentration gradient of the solute within the pores [29], and typically holds true at relatively high solute concentrations and when the pore size is significantly larger than the solute [30]. For the gyroid, a mono dimensional model for pore diffusion was assumed in the solid adsorbent, coupled with a mass balance to account for exchange of solute from the liquid solution to the adsorbent:

$$\frac{\partial q_t}{\partial t} = D_p \frac{\partial^2 C_p}{\partial x^2} \tag{5}$$

$$\frac{dC_t}{dt} = -\frac{A_a}{V_s}\int \frac{\partial q_t}{\partial t} dx \tag{6}$$

where C_p is the adsorbate concentration in the liquid-filled pores, D_p is the pore diffusivity, A_a is the adsorbent surface area, and x is the main transversal coordinate where diffusion occurs. A mono dimensional model was demonstrated to be effective to reproduce the uptake of the solute in complex geometries, reducing computational demands compared to more complex 3D models [30].

For the adsorbent beads, the same equations in spherical coordinates were employed:

$$\frac{\partial q_t}{\partial t} = D_p\left(\frac{\partial^2 C_p}{\partial r^2} + \frac{2}{r}\frac{\partial C_p}{\partial r}\right) \tag{7}$$

$$\frac{dC_t}{dt} = -\frac{V_a}{V_s}\frac{3}{r_p^3}\int \frac{\partial q_t}{\partial t} dr \tag{8}$$

where r_p is the average particle radius, and r is the radial coordinate of the spherical beads. These equations were solved and fitted to kinetic data as described in Sarwar *et al.,* assuming bulk solution concentration at the periphery and centre-line symmetry, in order to evaluate pore diffusivity for Sudan 1 and paclitaxel. [30] Sudan 1 and paclitaxel free diffusivity in solution, D_f, were estimated with the Stokes-Einstein equation [31], assuming spherical solutes.

2.8. Small scale cultivations and in situ recovery of taxadiene with 3D printed adsorbents

The best performing 3D printed adsorbent was used in microbial cultivations for in situ recovery of taxadiene from culture media.

Glycerol stocks were used to prepare *S. cerevisiae LRS5* colonies on agar. Pre cultures were prepared by transferring a single colony to 5 mL of fresh YP media (1 % yeast extract; 2 % peptone; 2 % glucose) and incubated overnight at 30 °C and 250 rpm. The following day, the cultivation was started by adding the sterile adsorbent into culture media (1 % yeast extract; 2 % peptone; 2 % galactose) and using an aliquot of the pre culture for inoculation to start the culture with an initial optical density (OD600) of 1.

The cultivations were carried out in 50 mL falcon tubes containing 5 mL of culture media and 3 % (v/v) concentration of adsorbent, and were incubated in an orbital shaker incubator (Eppendorf/Innova 42, Stevenage, UK) at 30 °C and 250 rpm for 3 days. The criteria of selecting 3 % (v/v) concentration of adsorbent came from the observations of Santoyo-Garcia *et al.* where they carried out *S. cerevisiae LRS5* cultivations using different concentrations of Diaion HP-20 beads and observed that 3 % (w/v) was the optimal concentration to maximize cell growth and taxadiene recovery [12]. Control experiments were carried out with Diaion HP-20 resin beads (3 % v/v) as benchmark and a culture with no adsorbent to assess cell growth and taxadiene recovery in these conditions.

2.9. Extraction and quantification of taxadiene

At the end of the cultivations, adsorbents and cells were separated to quantify taxadiene concentration and to analyse its distribution between the two fractions.

Cells were recovered by centrifugation of the culture media and subsequent separation of the precipitate (cells) from the supernatant (cell free media). Cells were gently dried with nitrogen gas to remove excess of water. Subsequently 5 mL of acetone was added to extract intracellular taxadiene by keeping the resulting mixture in a rotatory incubator for 24 hrs at 30 °C and 250 rpm.

Prior to taxadiene recovery, the adsorbents were washed twice with tween 80 solution (0.05 % v/v) to remove attached cells. Acetone was used to desorb and extract taxadiene from both the solid adsorbent and detached cells at a volume ratio of 1:1. Taxadiene extraction from cell free media was achieved using dodecane (as it is not miscible in water) with a volume ratio of 1:0.2. Volume ratio is defined as the ratio between the total cultivation volume and the extraction solvent.

Taxadiene was quantified by gas chromatography coupled with a mass spectrophotometer (GC–MS). 100 µL of the extraction samples were injected to the GC–MS, using a TRACE 1300 Gas Chromatography system, equipped with a TG-SQC column (15 m x 0.25 mm x 0.25 µm) and coupled to an ISQ LT single quadrupole mass spectrometer (Thermo Fisher Scientific, UK). The chromatographic separation and the mass spectra were obtained using the procedure described by Galindo-Rodriguez *et al.* [16].

After taxadiene quantification, cell pellets were dried at 80 °C for 24 h, and subsequently weighted to quantify the biomass produced on the different cultivations.

2.10. Statistical analysis

One-way ANOVA analysis was performed to investigate statistical significant differences on taxadiene cultivations in the presence of Diaion HP-20 beads, the 3D printed adsorbent, and no adsorbent (control). The null hypotheses claim that both the *S. cerevisiae* biomass and the concentration of taxadiene recovered are not influenced by the presence of the adsorber in the fermenter.

Tukey's honest significant different test was carried out to determine difference between groups. One-way ANOVA and Tukey's test were performed with a confidence level of 99 %, i.e. $p \leq 0.01$. All statistical analyses were performed in Microsoft Excel.

3. Results and discussion

3.1. Effect of porogen concentration and porogen composition on the pore structure of 3D printed materials

The nano-scale morphology of methacrylate porous polymers comprises interconnected clusters of aggregated globules [32]. The pore

structure in methacrylate monoliths, including 3D printed objects, can be controlled by porogen selection and by modulating the monomer/-porogen ratio in the resin composition [28,32–34]. The globular porous network for the 3D printed materials investigated is presented in the SEM images in Fig. 3, while their average pore size and pore size distribution are summarised in Table 2. The measured average pore size of Diaion HP-20 measured by the method described by Dong *et al.* [28] (45 nm) was on the same order as the value reported in literature (29 nm) [11], offering a cross-validation of the quality of this method.

Porogen concentration had a significant effect on the pore structure and pore size of the 3D printed materials. In particular, an increment of

Table 2
Physical properties of Diaion HP-20 and 3D printed materials.

Adsorbent	Average pore diameter (nm)	Density (g mL^{-1})	Surface area (m^2 mL^{-1})
Diaion HP-20	45.24	1.01	828.38
BEMA30	26.35	1.05 ± 0.0	104.92
BEMA40	80.40	0.77 ± 0.1	49.96
BEMA60	122.69	0.48 ± 0.0	16.95
BEMAP2	149.32	0.36 ± 0.0	25.07

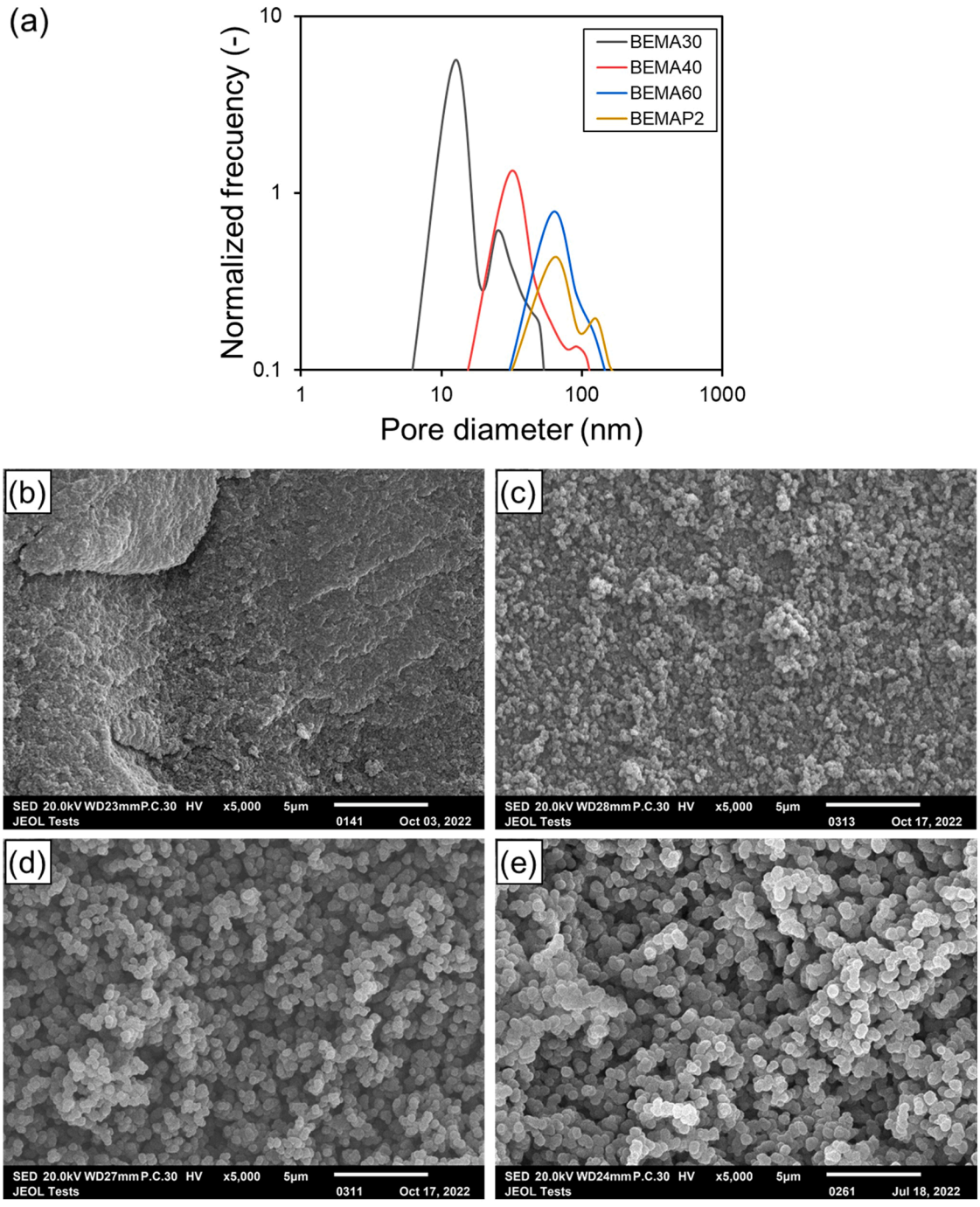

Fig. 3. (a) Pore size distributions of 3D printed adsorbents investigated in this work. SEM photographs at x5000 of 3D printed gyroid cubes fabricated with (b) BEMA30, (c) BEMA40, (d) BEMA60 and (e) BEMAP2.

porogen concentration from 30 to 60 % (v/v) produced an increase of the average pore size from 26 nm to 123 nm. This result is in agreement with other reports in which pore size increases with porogen concentration [32,34]. The porous structure of a polymer results from phase separation which occurs when the molecular size of the growing polymer exceeds its solubility limit in the reaction medium [35]. Phase separation results in the formation of nuclei which continue growing to form globules, followed by the aggregation of globules to form clusters [35]. Typically, low concentrations of porogens drive nucleation and the formation of micro-globules, eventually resulting in a closely packed material [34]. This mechanism is consistent with the results observed, with BEMA30, BEMA40 and BEMA60 progressively characterised by larger average pore sizes and larger polymeric globules, corresponding to progressively lower surface areas as the amount of porogen increased.

Porogen type also had an important influence on the resulting porous network of the 3D printed adsorbers. Despite both BEMA40 and BEMAP2 having been prepared with 40 % (v/v) porogen concentration, the latter had almost double average pore size than the former (149 nm vs 80 nm). This result is in accordance with Danquah and Forde who observed an increase in the average pore size of methacrylate monoliths from 395 to 2924 nm after increasing the concentration of DoOH in the co-porogen mixture from 10 to 50 % (v/v) [32]. Similarly, Dong *et al.* observed an increase in average pore size of 3D printed materials due to the gradual increment of 1-decanol concentration in the porogen mixture [28]. Porogens and co-porogens are traditionally classified as "good" or "bad" solvents, depending on their miscibility with the monomers and the growing polymeric chains [33]. The so-called bad solvents induce early phase separation, resulting in higher aggregation of globules and subsequent formation of larger clusters, ultimately producing a material with larger pores and lower surface area. The opposite effect occurs with good solvents, i.e. phase separation is delayed, leading to lower globule aggregation and formation of smaller clusters, characterised by smaller pores and higher surface area. These findings indicate that the porogen mixture with higher DoOH content (CP-2) has lower miscibility with the monomers in the resin composition (BEMA, BUMA and SR399) and phase separation occurred earlier during photopolymerisation, resulting in the formation of larger globules and with larger pores and smaller surface area [33].

3.2. Mass transfer study in 3D printed adsorbents, kinetic pore diffusion models

Adsorption kinetic experiments were carried out to study the performance of the 3D printed adsorbers to capture hydrophobic molecules, and to investigate mass transfer in materials with different pore structures. Sudan 1 and paclitaxel were used as proxy molecules for taxadiene due to ethical and financial restrictions on commercial taxadiene. Sudan 1 was selected as model molecule thanks to its hydrophobic nature and a similar molecular weight as taxadiene, while paclitaxel is the result of the enzymatic conversion of taxadiene. Commercial Diaion HP-20 beads were employed as benchmark adsorbent to assess the 3D printed adsorbents. Diaion HP-20 was selected as it is the material of preference for routine extraction of non-polar taxanes [13,36], taxadiene [12] and paclitaxel [37]. Fig. 4 shows the adsorption kinetic data of Sudan 1 and paclitaxel onto the 3D printed materials and the commercial resin Diaion HP-20. The adsorption kinetics of BEMA60 and BEMAP2 reached apparent equilibrium after 26 h. This was not the case with BEMA30 and BEMA40 which displayed slower uptake continuing after 26 h, attributed to diffusion resistance due to smaller pores in these materials. Diffusion resistance is usually associated with steric restrictions and interactions of the solute with the pore walls [31]. On the other hand, the adsorption of Sudan 1 and paclitaxel onto Diaion HP-20 reached equilibrium in approximately 2 h, indicative that pore diameter is not the only parameter influencing adsorption kinetics. It is worth noting that Diaion HP-20 beads have significantly smaller path length for solute diffusion (75–175 μm radius) compared to the 3D printed SG cubes (500 μm). Overall path length combined with surface area and the morphology of the porous network directly influence the adsorption process as this is usually controlled by diffusion in the stagnant liquid phase in the pores of the adsorbent [38,39]. In this regard, 3D printing enables the custom-made fabrication of hierarchical porous materials at the micro and nanoscale through CAD design and chemical composition to obtain tailored adsorbents with optimised performances[40].

The adsorption kinetics were preliminarily described with the PFO and PSO kinetic models and the obtained parameters are shown in Table 3. The PFO and PSO models lump all mass transfer and kinetic phenomena in a simple single term, the apparent rate constant, so they must be treated as qualitative indicators of the overall adsorption performance observed. The apparent rate constant in Diaion HP-20 was about one order of magnitude higher compared to the 3D printed adsorbers, further confirming the relevance of diffusion resistance in these materials.

To better understand mass transfer and take into consideration the different path lengths in the Diaion HP-20 beads and in the 3D printed adsorbers, the kinetic data were modelled with a more physically meaningful model which assumes pore diffusion as the limiting kinetic mechanism.

Table 3 summarises the pore diffusivity values normalized with the calculated free diffusivity in solution of Sudan 1 (2.3×10^{-6} cm^2/s) and

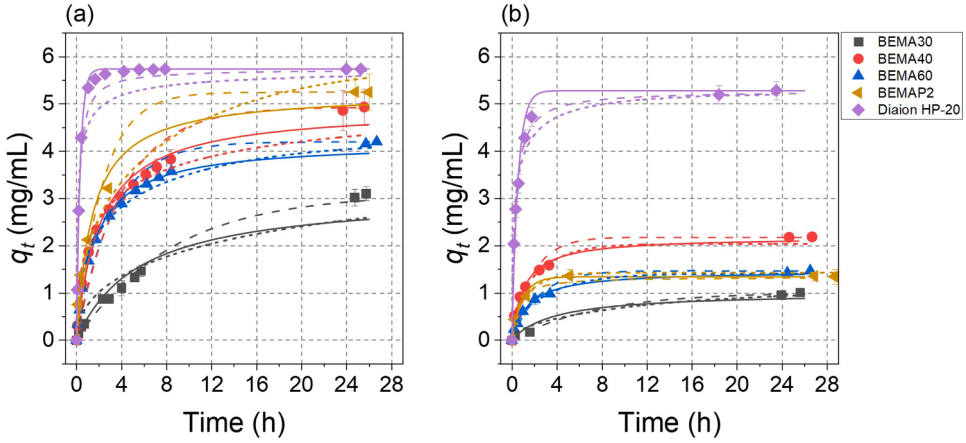

Fig. 4. Adsorption kinetics on the different 3D materials and on Diaion HP-20 for (a) Sudan 1 and (b) paclitaxel. All adsorption kinetics experiments were carried out with an initial concentration of Sudan 1 and paclitaxel of 100 ppm. The experimental data was fitted with the PFO (dashed lines), PSO (continuous line) and pore diffusion (dotted lines) models. Error bars represent mean standard deviation ($n = 3$).

Table 3
Estimated parameters of the PFO and PSO kinetic models as well as for the pore diffusion model for the adsorption of Sudan 1 and paclitaxel onto 3D printed materials and Diaion HP-20 beads.

SUDAN 1					
	Pseudo-first order		Pseudo-second order		Pore diffusion
	k_1 (h^{-1})	q_e (mg mL^{-1})	k_2 (mL mg^{-1} h^{-1})	q_e (mg mL^{-1})	D_p/D_f
BEMA30	0.1 ± 0.0	3.1 ± 0.1	0.1 ± 0.0	3.1 ± 0.1	0.212 ± 0.038
BEMA40	0.3 ± 0.0	4.9 ± 0.5	0.1 ± 0.0	4.9 ± 0.5	0.458 ± 0.081
BEMA60	0.3 ± 0.0	4.2 ± 0.0	0.1 ± 0.0	4.2 ± 0.0	0.747 ± 0.006
BEMAP2	0.4 ± 0.1	5.3 ± 0.4	0.1 ± 0.0	5.3 ± 0.4	0.872 ± 0.112
Diaion HP-20	3.0 ± 0.1	5.7 ± 0.0	0.9 ± 0.0	5.7 ± 0.0	0.202 ± 0.001
PACLITAXEL					
	Pseudo-first order (PFO)		**Pseudo-second order (PSO)**		**Pore diffusion**
	k_1 (h^{-1})	**q_e (mg mL^{-1})**	**k_2 (mL mg^{-1} h^{-1})**	**q_e (mg mL^{-1})**	**D_p/D_f**
BEMA30	0.1 ± 0.0	1.0 ± 0.1	0.3 ± 0.0	1.0 ± 0.1	0.145 ± 0.028
BEMA40	0.5 ± 0.0	2.2 ± 0.1	0.4 ± 0.0	2.2 ± 0.1	1.349 ± 0.054
BEMA60	0.4 ± 0.1	1.5 ± 0.0	0.5 ± 0.1	1.5 ± 0.0	0.631 ± 0.102
BEMAP2	1.1 ± 0.3	1.3 ± 0.2	1.5 ± 0.7	1.3 ± 0.2	1.150 ± 0.114
Diaion HP-20	1.9 ± 0.1	5.3 ± 0.2	0.6 ± 0.0	5.3 ± 0.2	0.369 ± 0.026

paclitaxel (1.6×10^{-6} cm^2/s). The adsorption kinetic data of Sudan 1 and paclitaxel, normalised to the initial concentration (100 ppm) and fitted with the pore diffusion model, are shown in Fig. 4.

In Sudan 1, there is a positive correlation between D_p and average pore size. On the other hand, D_p for paclitaxel exhibits no correlation with pore size. In addition, D_p for paclitaxel in BEMA40 and BEMAP2 were larger than unity, suggesting that solute transport inside the material is faster than its free diffusivity in solution. Considering that paclitaxel molecule is larger and presents more electronegative atoms in its structure in comparison to Sudan 1, it is possible that other transport mechanisms can be involved on its adsorption such as electrostatic potential driving forces [41]. The deviations between experimental data and the models were attributed to the combined effect of experimental error, the approximation on the free diffusivity of solutes using Stokes-Einstein equation and because the 1D diffusion model simplifies the complex diffusion phenomena that occurs in all three cartesian directions as well as neglects other mass transfer phenomena such as surface diffusion and film mass transfer.

The effect of pore size on diffusion was visually observed from cross section cuts of the gyroids used for adsorption of Sudan 1. Fig. 5 shows the outer and inner surface of 3D printed materials with different pore size. The outer surface in all materials exhibited an intense orange colour indicating saturation of Sudan 1. On the other hand, the colour tone in the inner sections of BEMA30 and BEMA40 were white or pale orange indicating that the solute did not diffuse completely through these materials and reach equilibrium after 26 h. One of the challenges

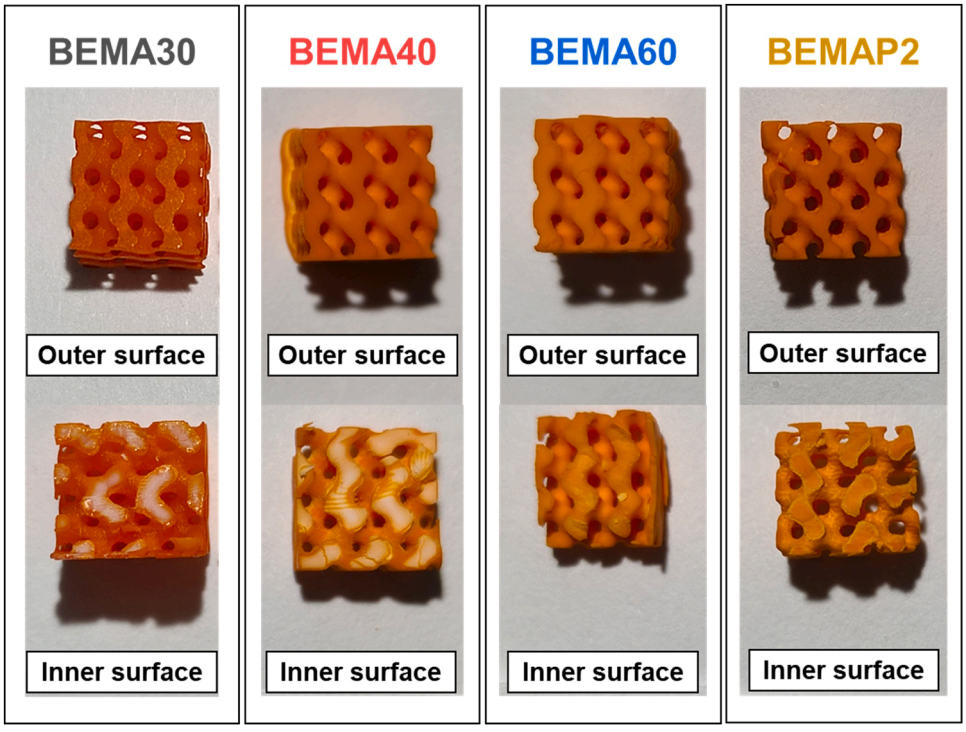

Fig. 5. Comparison of outer and inner surface of 3D printed materials used in Sudan 1 adsorption. The white or pale orange colour in the inner sections of BEMA30 and BEMA40 suggested hindered diffusion due to small pore size.

in DLP printing is the over-curing of the model during the printing process. Johnson *et al.* scanned 3D printed gyroids with X-ray computed tomography to obtain 3D images that were compared with the original CAD designs. They observed reduced porous channel diameter in the internal region of the 3D printed models [40]. It is possible that the 3D printed gyroids in this work presented certain degree of over-curing in the inner sections which resulted in smaller channels and consequently greater path length for diffusion and lower interconnections between pores.

The PFO and PSO models are extensively used to describe adsorption kinetic process and are easy to be applied [42]. However, these models are empirical and lack a clear physical meaning [43]. Pore diffusion values calculated for Diaion HP-20 were smaller compared to most 3D printed materials. Considering that Diaion HP-20 displayed the fastest adsorption kinetic data and significantly larger surface area, confirms that mass transfer is complex process that cannot be easily described with a single model. On the other hand, the integration of the pore diffusion with material characterization (pore size distribution and surface area) described better the mass transfer mechanism that governs the adsorption process on the different materials. Future work will be devoted to a complete understanding of the mass transfer and kinetic mechanisms associated with metabolite adsorption on 3D printed porous media.

The rate of taxadiene production in cultivations with *S. cerevisiae LRS5* is strongly correlated to cell growth kinetics which happens in the span of days [12]. Therefore, the diffusional properties of the 3D printed materials are not a limiting factor on their application for in situ recovery of taxadiene, with adsorption capacity (i.e. loading) being a more significant parameter for material evaluation.

3.3. Adsorption isotherms

Adsorption equilibrium experiments were performed to study the effect of pore size and surface area on the adsorption capacity of 3D printed materials. Results of the equilibrium experiments are presented in Fig. 6. Equilibrium data of Sudan 1 and paclitaxel was fitted using a linear isotherm model:

$$q_e = KC_e \tag{9}$$

where q_e and C_e are the loading of the solute in the adsorbent and the concentration of the solute in solution at equilibrium, respectively, and K is the association constant describing the affinity of the solute for the adsorbent, summarised in Table 4 for the materials investigated.

BEMA40 was the material which showed the highest affinity for both Sudan 1 and paclitaxel among all 3D printed materials tested. The association constant value for Sudan 1 adsorption on BEMA40 was 5.7, 3.6 and 2.4 fold higher in comparison to BEMA30, BEMAP2 and BEMA60, respectively. In paclitaxel adsorption, the K value of BEMA40 was 2.4, 2.4 and 1.8 fold higher in comparison to BEMA30, BEMAP2 and BEMA60, respectively. The fact that BEMA30 showed the lowest loading of Sudan 1 and paclitaxel despite displaying the largest surface area among the 3D materials suggests that a fraction of its pores was not accessible to the solute molecules and the diffusion in this material was significantly slower.

Table 4
Sudan 1 and paclitaxel isotherm parameters on 3D printed materials and Diaion HP-20.

	Sudan 1		Paclitaxel	
	K (-)	R^2	K (-)	R^2
Diaion HP-20	1338.4 ± 25.1	0.998	309.4 ± 1.7	0.976
BEMA30	71.0 ± 8.4	0.999	11.9 ± 0.8	0.975
BEMA40	416.5 ± 94.7	0.990	32.3 ± 0.6	0.993
BEMA60	170.0 ± 10.7	0.999	18.2 ± 0.3	0.989
BEMAP2	116.1 ± 17.5	0.998	13.4 ± 0.5	0.990

On the other hand, Diaion HP-20 showed higher adsorption capacity for both Sudan 1 and paclitaxel than any of the 3D printed materials considered. The association constant of the commercial beads was 3.2- and 9.6-fold in comparison to BEMA40 for Sudan 1 and paclitaxel, respectively. The higher association constant in Diaion HP-20 was attributed to its much larger surface area which is 16.6-fold larger than BEMA40, suggesting significant gains can be made by increasing surface area in the printed material through narrower channel walls.

Liu *et at.* observed that average pore size affected the adsorption capacity of divinylbenzene resins. In their results, they found that the loading capacity of smaller molecules was higher in resins with smaller pores, whereas resins with larger pores showed higher loading for larger solutes [44].

The results indicate that surface area plays an important role in the adsorption capacity of polymeric materials. There is a balancing act as the pore size directly influences the fraction of surface area that is available for adsorption. The exclusion of the solute to smaller pores reduces the active surface area of a material and consequently its loading capacity [45].

3.4. In situ recovery of taxadiene from S. cerevisiae cultivations using 3D printed adsorbents

BEMA40 showed the greatest adsorption capacity for Sudan 1 and paclitaxel among the 3D printed adsorbers investigated in this work.

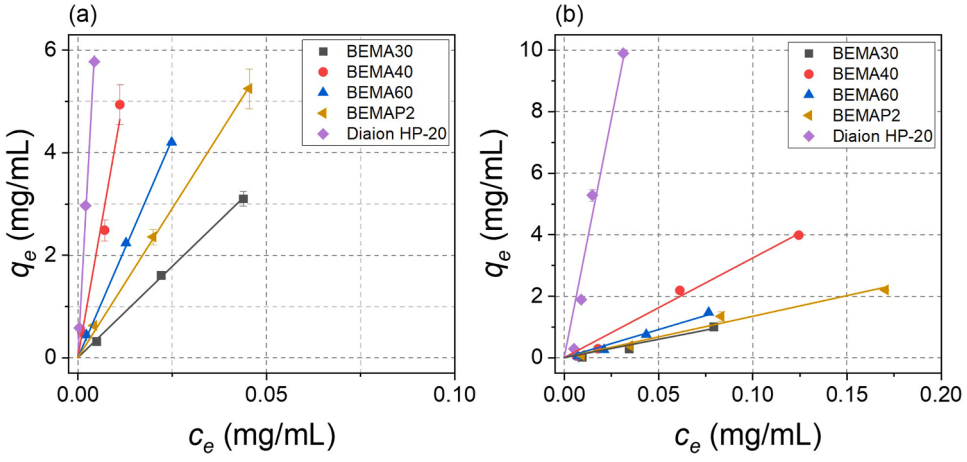

Fig. 6. Adsorption isotherms on the 3D printed materials investigated and Diaion HP-20 for Sudan 1 (a) and Paclitaxel (b). Values represent mean standard deviation ($n = 3$).

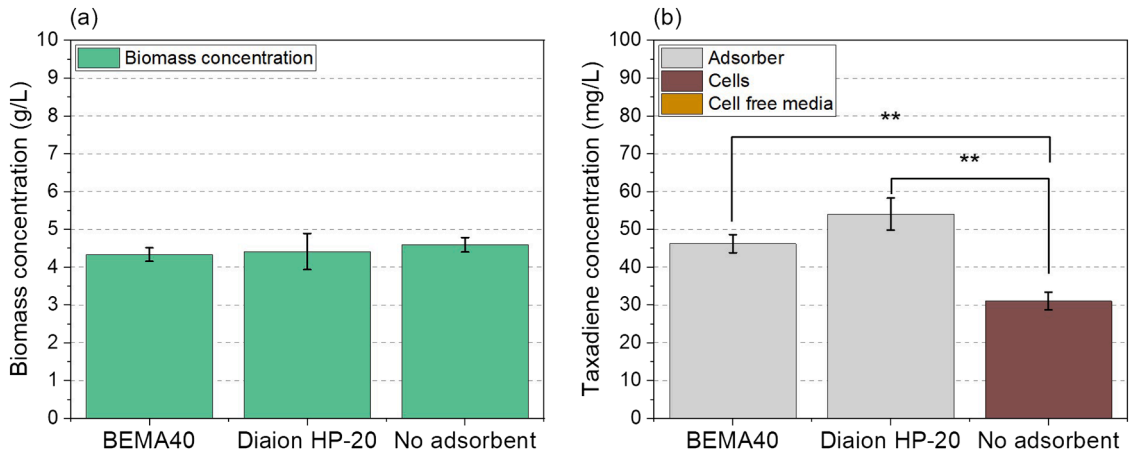

Fig. 7. Biomass (a) and taxadiene (b) concentration obtained in cultivations with BEMA40, Diaion HP-20 and no adsorbent control at small-scale (5 mL). Error bars represent mean standard deviation ($n = 3$) (**$p < 0.01$; Tukey's honest significant difference).

Further testing for in situ recovery of taxadiene in small-scale (5 mL) *S. cerevisiae* cultivations were carried out using 3 % (v/v) concentration of the 3D printed BEMA40 fabricated in the form of schoen gyroid cubes. Taxadiene and biomass concentrations obtained from the cultivation with the 3D-printed material were compared with cultivations using 3 % (v/v) Diaion HP-20 and the cultivation with no adsorbent. Negative controls consisted of incubating BEMA40 and Diaion HP-20 in no inoculated culture media to verify aseptic conditions. Adsorbent concentration was set to 3 % (v/v) to maximize cell growth and taxadiene titres as observed by Santoyo-Garcia *et al.* [12]. The results of biomass and taxadiene concentrations on BEMA40, Diaion HP-20 and no adsorbent cultivations are presented in Fig. 7.

The addition of BEMA40 and Diaion HP-20 had no effect on cell growth compared to a cultivation with no adsorbent (Fig. 7a), as also confirmed by one-way ANOVA ($p = 0.72$). Therefore, the presence of the adsorbers in the cultivations did not affect cell growth, in agreement with previous results using the same microorganism [12]. Biocompatibility can be defined as the ability of a material to perform properly without affecting the biological host [46]. By this definition, we can conclude that BEMA40 is a biocompatible adsorbent to recover taxadiene in *S. cerevisiae* cultivations.

Taxadiene titres at the end of the cultivations were 46 ± 2, 54 ± 4 and 31 ± 2 mg/L for BEMA40, Diaion HP-20 and no adsorbent, respectively. One-way ANOVA analysis indicated significant difference between the three groups with a confidence level of 99 % ($p = 0.001$). Tukey's test was used to determine the difference between groups. Tukey criterion ($T = 14$) with a confidence level of 99 % indicated that taxadiene concentration in the no adsorbent culture was significantly different from cultures with Diaion HP-20 and BEMA40.

Taxadiene loadings on the adsorbent materials were 1.0 ± 0.1 and 1.2 ± 0.1 on BEMA40 and Diaion HP-20 respectively, indicating no significant difference in the recovery of taxadiene between the two adsorbents. In other words, the 3D printed material performed as good as the commercial material despite the different association constants obtained in the characterization experiments with Sudan 1 and paclitaxel. It is worth noting that the 3D printed adsorbent material here presented is a first-of-its-kind, with reasonable improvements in adsorption performances achievable through optimisation of the formulation and of the 3D printing settings [19]. In addition, the design freedom of 3D printing enables fabrication of adsorbents that can be adapted to diverse bioreactor types such as rotating bed reactor, external recirculation columns, etc. Such 3D printed adsorbents can be designed to minimise shear stress on the adherent cells, improve flow distribution within the bioreactor and have customized chemistry and pore structure to fit the requirements of bespoke operations in biotechnology. All of these considerations suggest the opportunities of 3D printed adsorbents to overcome the limited performances of traditional bead-based adsorbents.

Future opportunities for 3D printed adsorbents mostly relate to development of new materials and 3D printing methods. The first one highlights the need to provide for materials fully compatible with additive manufacturing technologies and with specific properties for applications in adsorption, separation and purification processes [26]. On the other hand, it is expected that improvement of 3D printers and resins formulations will reduce printing times, scalability and ease the fabrication of structures with finely controlled features at high resolution (<1 μm) [19].

4. Conclusions

We successfully 3D-printed materials with controllable pore structure by tailoring porogen composition and concentration, and demonstrated that pore size in 3D printed materials can be modulated with the porogen concentration in the resin mixture. This approach expands the possibilities to control the pore structure in 3D printing with photopolymer resins.

The analysis of SEM photographs revealed that decreasing the porogen content from 60 % to 30 % (v/v) reduced the average pore diameter from 123 nm to 26 nm. The material with the smaller average pore diameter (BEMA30) showed lower adsorption rate and capacity, suggesting that a fraction of its pores was not accessible for adsorption. On the other hand, the material prepared with 40 % porogen (BEMA40) displayed the highest adsorption capacity for Sudan 1 and paclitaxel.

BEMA40 was tested and compared with commercial Diaion HP-20 beads for the *in situ* recovery of taxadiene in small-scale (5 mL) cultivations. Taxadiene concentration on BEMA40 and Diaion HP-20 were 46 ± 2 and 55 ± 4 mg/L, respectively. Biomass concentration obtained in the culture with BEMA40 and the control with no adsorbent were 4.4 and 4.6 g/L, respectively. These results indicated that the presence of the 3D material did not affect cell growth in these conditions and demonstrated for the first time the potential of 3D printed materials to recover biological products. Furthermore, the relative ease to fabricate 3D printed materials and the design freedom open the possibility to explore their implementation in different bioreactor types and to explore more applications in bioprocesses. Future advances in 3D printing technologies coupled with optimisation of 3D printable formulations hold a further promise for adsorption materials and adsorption processes with improved performances.

Funding

This work was funded by the Mexican National Council of Humanities, Sciences and Technologies (CONHACYT). Scholarship reference: 2018–000009–01EXTF-00060.

CRediT authorship contribution statement

Giuseppe Rafael Galindo-Rodriguez: Writing – review & editing, Writing – original draft, Visualization, Methodology, Investigation, Formal analysis, Data curation, Conceptualization. **M. Sulaiman Sarwar:** Writing – review & editing, Software. **Leonardo Rios-Solis:** Writing – review & editing, Resources. **Simone Dimartino:** Writing – review & editing, Supervision, Resources, Project administration, Funding acquisition.

Declaration of competing interest

The authors declare that they have no known competing financial interests or personal relationships that could have appeared to influence the work reported in this paper.

Data availability

Data will be made available on request.

Acknowledgements

The authors would like to thank and appreciate the support of the IbioE technicians Katalin Kis, Eve Duncan and Mark Lauchlan. We also thank Stuart Martin for his collaboration with the GCMS analysis.

Supplementary materials

Supplementary material associated with this article can be found, in the online version, at doi:10.1016/j.chroma.2024.464815.

References

[1] Y.-H.P. Zhang, J. Sun, Y. Ma, Biomanufacturing: history and perspective, J. Ind. Microbiol. Biotechnol. 44 (2017) 773–784, https://doi.org/10.1007/s10295-016-1863-2.
[2] L.E. Walls, et al., Optimizing the biosynthesis of oxygenated and acetylated Taxol precursors in Saccharomyces cerevisiae using advanced bioprocessing strategies, Biotechnol. Bioeng. 118 (1) (2021) 279–293, https://doi.org/10.1002/bit.27569.
[3] S.L. Chen, H. Yu, H.M. Luo, Q. Wu, C.F. Li, A. Steinmetz, Conservation and sustainable use of medicinal plants: problems, progress, and prospects, Chin. Med. (United Kingdom) 11 (1) (2016) 1–10, https://doi.org/10.1186/S13020-016-0108-7/TABLES/5.
[4] E. Carsanba, M. Pintado, C. Oliveira, Fermentation strategies for production of pharmaceutical terpenoids in engineered yeast, Pharmaceuticals 14 (4) (2021) 295, https://doi.org/10.3390/PH14040295.
[5] J. Wong, L. Rios-Solis, J.D. Keasling, Microbial production of isoprenoids, Conseq. Microb. Interact. Hydrocarbons, Oils, Lipids (2017) 359–382, https://doi.org/10.1007/978-3-319-50436-0_219.
[6] L.E. Walls, L. Rios-Solis, Sustainable production of microbial isoprenoid derived advanced Biojet fuels using different generation Feedstocks: a review, Front. Bioeng. Biotechnol. 8 (2020) 599560, https://doi.org/10.3389/FBIOE.2020.599560/BIBTEX.
[7] B. Nowrouzi, et al., Enhanced production of taxadiene in Saccharomyces cerevisiae, Microb. Cell Fact. 19 (1) (2020) 1–12, https://doi.org/10.1186/s12934-020-01458-2.
[8] V. Rajamanickam, C. Herwig, O. Spadiut, Z. Zajickov, Monoliths in bioprocess technology, Chromatography 2 (2) (2015) 195–212, https://doi.org/10.3390/CHROMATOGRAPHY2020195.
[9] L.E. Walls, J.L. Martinez, E.A. del Rio Chanona, L. Rios-Solis, Definitive screening accelerates Taxol biosynthetic pathway optimization and scale up in Saccharomyces cerevisiae cell factories, Biotechnol. J. 17 (1) (2022) 2100414, https://doi.org/10.1002/BIOT.202100414.
[10] J.T. Dafoe, A.J. Daugulis, In situ product removal in fermentation systems: improved process performance and rational extractant selection, Biotechnol. Lett. 36 (3) (2014) 443–460, https://doi.org/10.1007/S10529-013-1380-6/FIGURES/1.
[11] T. Phillips, et al., Use of in situ solid-phase adsorption in microbial natural product fermentation development, J. Ind. Microbiol. Biotechnol. 40 (5) (2013) 411–425, https://doi.org/10.1007/S10295-013-1247-9.
[12] J.H. Santoyo-Garcia, et al., In situ solid-liquid extraction enhances recovery of taxadiene from engineered Saccharomyces cerevisiae cell factories, Sep. Purif. Technol. 290 (2022) 1383–5866, https://doi.org/10.1016/J.SEPPUR.2022.120880.
[13] J.H. Santoyo-Garcia, et al., The synergetic effect from the combination of different adsorption resins in batch and semi-continuous cultivations of S. Cerevisiae cell factories to produce acetylated Taxanes precursors of the anticancer drug Taxol, Biotechnol. Bioeng. 120 (8) (2023) 2160–2174, https://doi.org/10.1002/BIT.28487.
[14] M. Othman, A.B. Ariff, M.R. Kapri, L. Rios-Solis, M. Halim, Growth enhancement of probiotic pediococcus acidilactici by extractive fermentation of lactic acid exploiting anion-exchange resin, Front. Microbiol. 9 (2018) 2554, https://doi.org/10.3389/FMICB.2018.02554/BIBTEX.
[15] S.N.H. Oslan, et al., Integrated stirred-tank bioreactor with internal adsorption for the removal of ammonium to enhance the cultivation performance of gdhA derivative Pasteurella multocida B:2, Microorganisms 8 (11) (2020) 1654, https://doi.org/10.3390/MICROORGANISMS8111654.
[16] G.R. Galindo-Rodriguez, J.H. Santoyo-Garcia, L. Rios-Solis, S. Dimartino, In situ recovery of taxadiene using solid adsorption in cultivations with Saccharomyces cerevisiae, Prep. Biochem. Biotechnol. (2023), https://doi.org/10.1080/10826068.2023.2207204/SUPPL_FILE/LPBB_A_2207204_SM4827.DOCX.
[17] F. Rezaei, P. Webley, Optimum structured adsorbents for gas separation processes, Chem. Eng. Sci. 64 (24) (2009) 5182–5191, https://doi.org/10.1016/J.CES.2009.08.029.
[18] L.C.T. Scorza, U. Simon, M. Wear, A. Zouliatis, S. Dimartino, A.J. McCormick, Evaluation of novel 3D-printed monolithic adsorbers against conventional chromatography columns for the purification of c-phycocyanin from Spirulina, Algal. Res. 55 (2021) 102253, https://doi.org/10.1016/J.ALGAL.2021.102253.
[19] M. Conti, et al., Porous platform inks for fast and high-resolution 3D printing of stationary phases for downstream processing, Adv. Mater. Technol. (2023) 2300801, https://doi.org/10.1002/ADMT.202300801.
[20] J. Zhang, Q. Hu, S. Wang, J. Tao, M. Gou, Digital light processing based three-dimensional printing for medical applications, Int. J. Bioprint. 6 (1) (2020) 12–27, https://doi.org/10.18063/IJB.V6I1.242.
[21] K.V. Wong, A. Hernandez, A review of additive manufacturing, Int. Scholarly Res. Netw. ISRN Mech. Eng. 2012 (2012), https://doi.org/10.5402/2012/208760.
[22] R. Chaudhary, P. Fabbri, E. Leoni, F. Mazzanti, R. Akbari, C. Antonini, Additive manufacturing by digital light processing: a review, Progr. Addit. Manuf. 2022 (2022) 1–21, https://doi.org/10.1007/S40964-022-00336-0.
[23] E. Andrzejewska, Free radical photopolymerization of multifunctional monomers, Three-Dimens. Microfabric. Using Two-Photon Polym. (2016) 62–81, https://doi.org/10.1016/B978-0-323-35321-2.00004-2.
[24] M. Lang, S. Hirner, F. Wiesbrock, P. Fuchs, A review on modeling cure kinetics and mechanisms of photopolymerization, Polymers 14 (10) (2022) 2074, https://doi.org/10.3390/POLYM14102074.
[25] C. Yu, et al., Photopolymerizable biomaterials and light-based 3D printing strategies for biomedical applications, Chem. Rev. 120 (19) (2020) 10695–10743, https://doi.org/10.1021/ACS.CHEMREV.9B00810/ASSET/IMAGES/MEDIUM/CR9B00810_M007.GIF.
[26] S. Dimartino, et al., Flexible material formulations for 3D printing of ordered porous beds with applications in bioprocess engineering, Bioresour. Bioprocess. 9 (1) (2022) 1–8, https://doi.org/10.1186/S40643-022-00511-9/FIGURES/4.
[27] U. Simon, S. Dimartino, Direct 3D printing of monolithic ion exchange adsorbers, J. Chromatogr. A 1587 (2019) 119–128, https://doi.org/10.1016/J.CHROMA.2018.12.017.
[28] Z. Dong, et al., 3D printing of inherently nanoporous polymers via polymerization-induced phase separation, Nat. Commun. 2021 12:1 12 (1) (2021) 1–12, https://doi.org/10.1038/s41467-020-20498-1.
[29] W.D. Chen, X.Y. Dong, Y. Sun, Analysis of diffusion models for protein adsorption to porous anion-exchange adsorbent, J. Chromatogr. A 962 (1–2) (2002) 29–40, https://doi.org/10.1016/S0021-9673(02)00466-1.
[30] M.S. Sarwar, U. Simon, S. Dimartino, Experimental investigation and mass transfer modelling of 3D printed monolithic cation exchangers, J. Chromatogr. A 1646 (2021), https://doi.org/10.1016/J.CHROMA.2021.462125.
[31] P. Dechadilok, W.M. Deen, Hindrance factors for diffusion and convection in pores, Ind. Eng. Chem. Res. 45 (21) (2006) 6953–6959, https://doi.org/10.1021/IE051387N/ASSET/IMAGES/LARGE/IE051387NF00007.JPEG.
[32] M.K. Danquah, G.M. Forde, Preparation of macroporous methacrylate monolithic material with convective flow properties for bioseparation: investigating the kinetics of pore formation and hydrodynamic performance, Chem. Eng. J. 140 (1–3) (2008) 593–599, https://doi.org/10.1016/J.CEJ.2008.02.012.
[33] M.H. Mohamed, L.D. Wilson, Porous copolymer resins: tuning pore structure and surface area with non reactive porogens, Nanomaterials 2 (2) (2012) 163, https://doi.org/10.3390/NANO2020163.
[34] Y.W. Chan, T. Kansil, C.M. Ongkudon, Analytical and preparative polymethacrylate monolith fabrication: effect of porogen content and column size on pore morphology, Colloid. Polym. Sci. 295 (12) (2017) 2373–2382, https://doi.org/10.1007/S00396-017-4213-7/FIGURES/11.
[35] F. Svec, J.M.J. Fréchet, Temperature, a simple and efficient tool for the control of pore size distribution in macroporous polymers, Macromolecules 28 (22) (1995) 7580–7582, https://doi.org/10.1021/MA00126A044/ASSET/MA00126A044.FP.PNG_V03.

[36] M. Shirshekanb, H. Rezadoost, M. Javanbakht, A.R. Ghassempour, The combination process for preparative separation and purification of paclitaxel and 10-deacetylbaccatin III using Diaion® Hp-20 followed by hydrophilic interaction based solid phase extraction, Iran. J. Pharm. Res. 16 (4) (2017) 1396. Accessed: Mar. 01, 2024. [Online]. Available: /pmc/articles/PMC5843301/.
[37] D.Y. Kang, J.H. Kim, Ultrasonic cavitation bubble-assisted adsorption of paclitaxel from cell-free culture supernatants of Taxus chinensis onto Diaion HP-20, Biotechnol. Bioprocess Eng. 28 (4) (2023) 577–588, https://doi.org/10.1007/S12257-023-1081-5/METRICS.
[38] H. Qiu, L. Lv, B.C. Pan, Q.J. Zhang, W.M. Zhang, Q.X. Zhang, Critical review in adsorption kinetic models, J. Zhejiang Univ. 10 (5) (2009) 716–724, https://doi.org/10.1631/JZUS.A0820524/METRICS.
[39] T.J. Levario, M. Dai, W. Yuan, B.D. Vogt, D.R. Nielsen, Rapid adsorption of alcohol biofuels by high surface area mesoporous carbons, Microporous Mesoporous Mater. 148 (1) (2012) 107–114, https://doi.org/10.1016/J.MICROMESO.2011.08.001.
[40] T.F. Johnson, et al., Evaluating 3D-printed bioseparation structures using multi-length scale tomography, Anal. Bioanal. Chem. (2023) 1–11, https://doi.org/10.1007/S00216-023-04866-6/FIGURES/8.
[41] M.C. Stone, G. Carta, Protein adsorption and transport in agarose and dextran-grafted agarose media for ion exchange chromatography, J. Chromatogr. A 1146 (2) (2007) 202–215, https://doi.org/10.1016/J.CHROMA.2007.02.041.
[42] J. Zhang, Physical insights into kinetic models of adsorption, Sep. Purif. Technol. 229 (2019) 115832, https://doi.org/10.1016/J.SEPPUR.2019.115832.
[43] J. Wang, X. Guo, Adsorption kinetic models: physical meanings, applications, and solving methods, J. Hazard. Mater. 390 (2020), https://doi.org/10.1016/J.JHAZMAT.2020.122156.
[44] W. Liu, Y. Zhang, S. Wang, L. Bai, Y. Deng, J. Tao, Effect of pore size distribution and amination on adsorption capacities of polymeric adsorbents, Molecules 26 (17) (2021) 5267, https://doi.org/10.3390/MOLECULES26175267.
[45] S.J. Reich, et al., Hindrance factor expression for diffusion in random mesoporous adsorbents obtained from pore-scale simulations in physical reconstructions, Ind. Eng. Chem. Res. 57 (8) (2018) 3031–3042, https://doi.org/10.1021/ACS.IECR.7B04840/ASSET/IMAGES/LARGE/IE-2017-04840W_0010.JPEG.
[46] S. Winkler, K.V. Meyer, C. Heuer, C. Kortmann, M. Dehne, J. Bahnemann, In vitro biocompatibility evaluation of a heat-resistant 3D printing material for use in customized cell culture devices, Eng. Life Sci. 22 (11) (2022) 699–708, https://doi.org/10.1002/ELSC.202100104.